

Controllable p-Type Doping of 2D WSe₂ via Vanadium Substitution

Azimkhan Kozhakhmetov, Samuel Stolz, Anne Marie Z. Tan, Rahul Pendurthi, Saiphaneendra Bachu, Furkan Turker, Nasim Alem, Jessica Kachian, Saptarshi Das, Richard G. Hennig, Oliver Gröning, Bruno Schuler, and Joshua A. Robinson*

Scalable substitutional doping of 2D transition metal dichalcogenides is a prerequisite to developing next-generation logic and memory devices based on 2D materials. To date, doping efforts are still nascent. Here, scalable growth and vanadium (V) doping of 2D WSe₂ at front-end-of-line and backend-of-line compatible temperatures of 800 and 400 °C, respectively, is reported. A combination of experimental and theoretical studies confirm that vanadium atoms substitutionally replace tungsten in WSe₂, which results in p-type doping via the introduction of discrete defect levels that lie close to the valence band maxima. The p-type nature of the V dopants is further verified by constructed field-effect transistors, where hole conduction becomes dominant with increasing vanadium concentration. Hence, this study presents a method to precisely control the density of intentionally introduced impurities, which is indispensable in the production of electronic-grade wafer-scale extrinsic 2D semiconductors.

1. Introduction

Doping transition metal dichalcogenides (TMDCs) is one of the major routes to realize next-generation logic transistors with ultimate gate length scaling. Both intrinsic and extrinsic TMDCs have been actively explored as a channel material at front-end-of-line (FEOL)^[1-4] and as a diffusion barrier, liner, and thin-film

transistor at back-end-of-line (BEOL)[5-7] for advanced semiconductor technology nodes. To date, wafer-scale synthesis of near electronic-grade intrinsic TMDCs has been successfully realized at FEOL (>700 °C)[8-10] and BEOL(<500 °C)[11-14] compatible temperatures. However, while various doping techniques can tune the electrical conductivity of TMDCs (e.g., surface charge transfer doping,[15] electrostatic doping,[16] intercalation,[17] and substitutional doping,[18,19]) progress is still limited in truly scalable doping. Furthermore, even though "proof-of-concept" devices have been demonstrated based on doped TMDCs including vanadium dopants, [20-24] uniform distribution and precise control of the impurity density over a large scale and use of methods compatible with the state-of-the-art Si CMOS 300 mm process

lines, still remains challenging.^[19,25,26] Thus, scalable doping of TMDCs at a large temperature window with accurate control over the doping concentration is urgently needed.

Here, we report controlled substitutional vanadium doping of WSe₂ films realized via metalorganic chemical vapor deposition (MOCVD) at BEOL and FEOL compatible temperatures using W(CO)₆, H_2 Se, and $(C_5H_5)_2$ V as metal, chalcogen, and dopant

A. Kozhakhmetov, S. Bachu, F. Turker, N. Alem, S. Das, J. A. Robinson Department of Materials Science and Engineering The Pennsylvania State University University Park, PA 16802, USA E-mail: jrobinson@psu.edu

S. Stolz, O. Gröning, B. Schuler nanotech@surfaces Laboratory

Empa-Swiss Federal Laboratories for Materials Science and Technology Dübendorf 8600, Switzerland

A. M. Z. Tan

School of Mechanical and Aerospace Engineering Nanyang Technological University

Singapore 639798, Singapore A. M. Z. Tan, R. G. Hennig

Department of Materials Science and Engineering University of Florida

Gainesville, FL 32611, USA

The ORCID identification number(s) for the author(s) of this article can be found under https://doi.org/10.1002/adfm.202105252.

DOI: 10.1002/adfm.202105252

R. Pendurthi, S. Das Department of Engineering Science and Mechanics The Pennsylvania State University University Park, PA 16802, USA

N. Alem, S. Das Materials Research Institute The Pennsylvania State University University Park, PA 16802, USA

N. Alem, J. A. Robinson Two-Dimensional Crystal Consortium The Pennsylvania State University University Park, PA 16802, USA

J. Kachian Intel Corporation 2200 Mission College Blvd Santa Clara, CA 95054, USA

J. A. Robinson Center for 2-Dimensional and Layered Materials The Pennsylvania State University University Park, PA 16802, USA

ADVANCED FUNCTIONAL MATERIALS

www.advancedsciencenews.com www.afm-journal.de

sources, respectively. Accurate tuning of the partial pressures of the reactants allows the synthesis of V-doped WSe2 with predetermined vanadium concentration, as verified by high-resolution X-ray photoelectron spectroscopy (XPS). Furthermore, room temperature Raman and photoluminescence (PL) spectroscopy studies reveal a strong dopant concentration dependence of the spectra where defect activated modes increase in intensity and positive trions are formed that completely quench the PL spectra. Atomic-scale characterization techniques such as aberration corrected scanning transmission electron microscopy (STEM), scanning tunneling microscopy and spectroscopy (STM/STS), and density functional theory (DFT) calculations reveal that vanadium atoms substitutionally replace W atoms in the WSe₂ lattice and introduce multiple defect states that are in close proximity to the valence band edge. The p-type nature of the vanadium dopants is further confirmed with back-gated field-effect transistors that exhibit an enhanced p-branch (hole) current and a positive threshold shift. Our systematic study provides substantial progress and fundamental insight in largescale synthesis of extrinsic 2D TMDCs with precisely controlled dopant concentrations that will be a major step toward successful integration with Si CMOS at FEOL and BEOL.

2. Results and Discussion

Pristine and V-doped FEOL compatible WSe₂ is synthesized on c-plane sapphire substrates at 800 °C and 700 Torr using W(CO)₆, V(C₅H₅)₂, and H₂Se, respectively.^[8,18] The introduction of vanadium atoms has a direct impact on the surface morphology of the obtained films, which are fully coalesced and primarily monolayer with some secondary-islands on top. (**Figure 1**a,b). The domain size is 800–900 nm in extrinsic films, where the introduction of vanadium dopants leads to a deviation from the traditional triangular shape for intrinsic WSe₂,

becoming truncated triangles and hexagons (Figure S1a-d, Supporting Information). Furthermore, an increase in density of bilayer islands occurs in extrinsic films with increasing dopant concentration (Figure S1c,d, Supporting Information), suggesting that vanadium adatoms serve as secondary nucleation centers on the surface. [18] In parallel, BEOL-compatible WSe2 is obtained on SiO₂/Si substrates at 400 °C and 700 Torr, with all films being coalesced, multilayer, and polycrystalline with an average domain size of 100 nm and an average thickness of 2.11 nm, corresponding to 3-4 layers (Figures S2a-d and S3a,b, Supporting Information).^[11] Moreover, chemical composition analysis via XPS indicates that V is incorporated into the WSe₂ lattice at both FEOL and BEOL temperatures.^[27] Both intrinsic and extrinsic FEOL films exhibit characteristic W 4f_{7/2}, W 4f_{5/2}, and W $5p_{3/2}$ peaks at 32.6, 34.8, and 38.1 eV and Se $3d_{5/2}$ and Se 3d_{3/2} peaks at 54.8 and 55.7 eV, respectively (Figure 1c and Figure S4a, Supporting Information) agreeing with previous reports. [18,28] As the vanadium concentration increases, associated V 2p_{3/2} and V 2p_{1/2} XPS peaks are detectable at 513.7 and 521.7 eV, respectively, corresponding to V-Se bonding and indicating successful doping of the WSe2 with V atoms (Figure 1d and Figure S3b, Supporting Information).^[29] Moreover, a peak at ≈517.0 eV is observed that corresponds to V-O bonding, and suggests vulnerability of extrinsic films toward oxidation (Figure 1d and Figure S4b, Supporting Information). [30,31] We observe similar characteristic W 4f, Se 3d, and V 2p peaks in XPS on BEOL V-WSe2 on SiO2/Si, where the dopant concentration varies as a function of the vanadium precursor flow rate (Figure S5a,b, Supporting Information).

Vanadium doping leads to enhancement in Raman defect modes and quenching of WSe₂ PL. Intrinsic and extrinsic FEOL compatible films exhibit peaks at 249.3 and 260.6 cm⁻¹ corresponding to A+E and 2 LA(M) characteristic in-plane and out-of-plane Raman active modes of 2D WSe₂.^[32,33] Intensified defect activated modes (ZA(M) (109.2 cm⁻¹) and LA(M) (128.6 cm⁻¹))

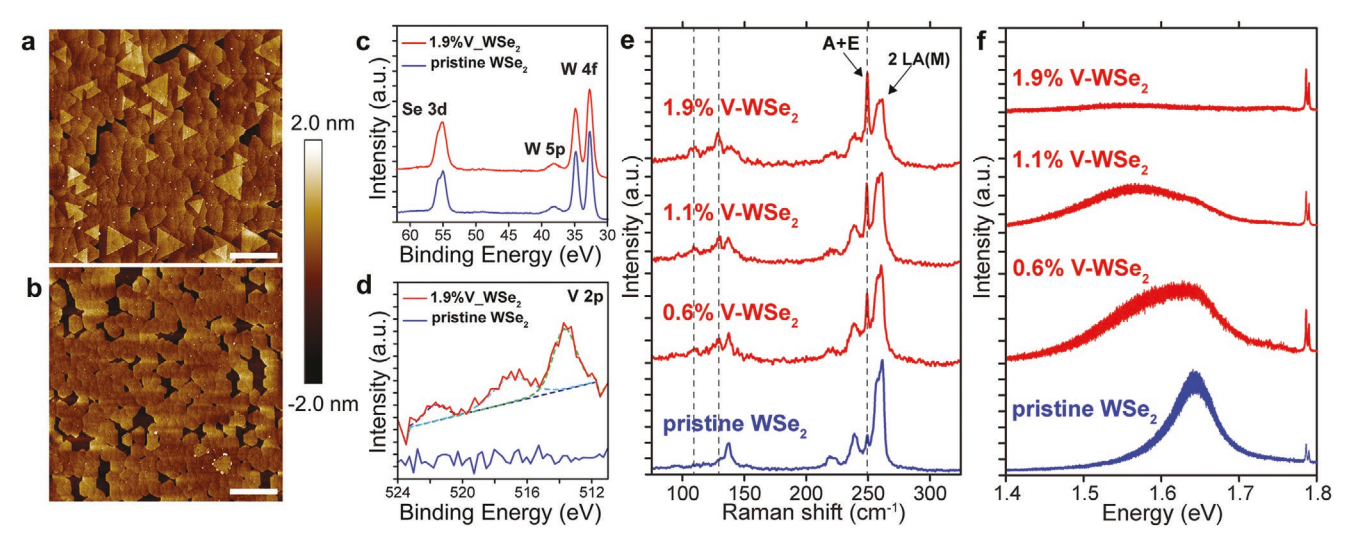


Figure 1. Surface morphology, chemical composition, and optical properties of pristine and V-doped FEOL WSe₂ films on sapphire substrates. AFM images of a) pristine and b) 1.9% vanadium doped WSe₂ films demonstrating a clear impact of the dopants on the surface morphology (1 μm scale bar). c,d) High-resolution XPS analysis further confirms the presence of vanadium atoms in the lattice where V 2p spectra are found at 513.7, 517.0, and 521.7 eV. e,f) Corresponding Raman spectra display increased density of defect activated modes whereas PL spectra start to redshift and are completely quenched (1.9% V—WSe₂) as a function of vanadium concentration, respectively.

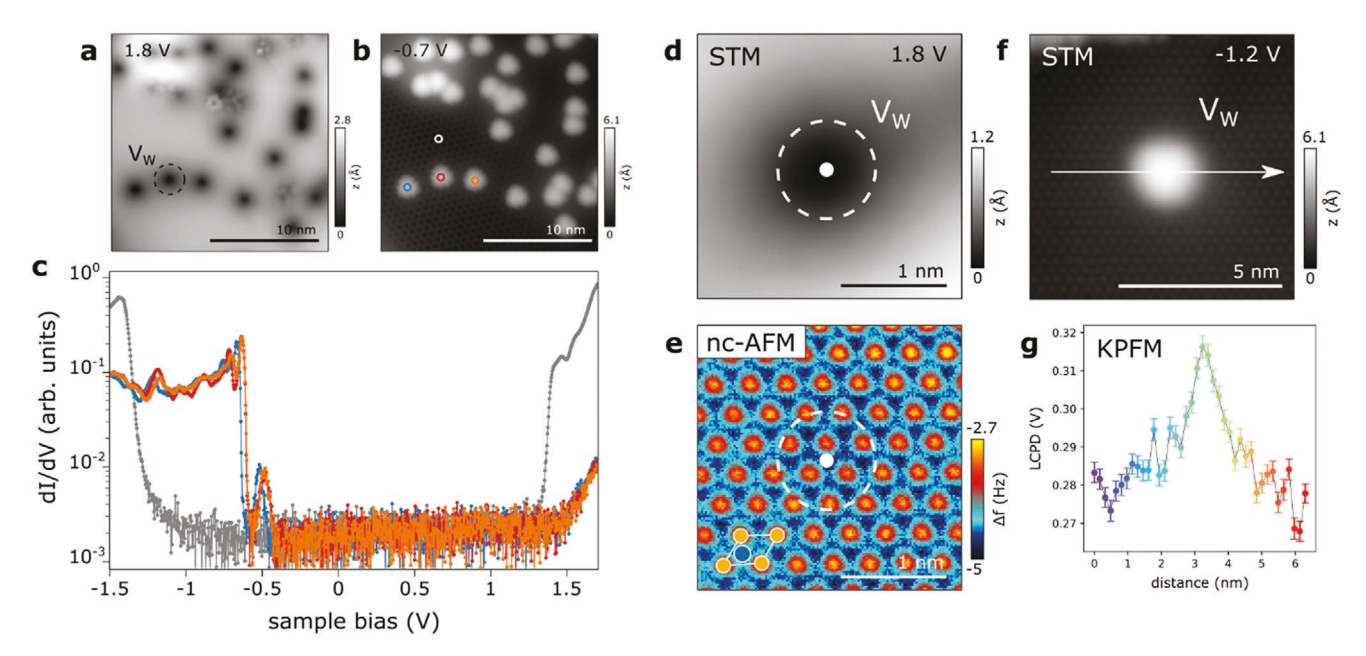


Figure 2. a,b) STM images of V-doped WSe₂ on EG/SiC at the same location at positive (V = 1.8 V) and negative (V = -0.7 V) sample bias. Multiple V_W dopants at various separations can be recognized. c) Differential conductance (dI/dV) spectra measured on three V_W dopants in color (locations indicated by circles in b) and the bare WSe₂ in gray. The spectra feature a series of p-type defect states above the valence band edge. d,e) STM and CO-tip nc-AFM image of a single V substituent at a W site. The V_W position is marked by a white dot. The unit cell is indicated at the bottom left in (e) (W = blue, Se = orange). f) STM image of V_W at negative (V = -1.2 V) sample bias. g) KPFM measurement across the V_W defect (along arrow in f) exhibiting a positive shift of the LCPD, indicative of a negative defect charge.

are the direct result of the increased disorder in the WSe2 lattice due to the introduction of vanadium and their intensity can serve as measure for the dopant concentration. [34,35] The corresponding PL spectra exhibit a similar dopant concentration dependence where intrinsic WSe₂ displays a 1.65 eV optical band gap, while V-WSe₂ is redshifted by 40 (0.6% V-WSe₂) and 80 meV (1.1% V-WSe₂) with reduced PL intensity. As the dopant concentration increases to 1.9%, there is a complete quench in the PL. The observed PL quenching is hypothesized to be due to an increased density of positive trions because vanadium is expected to be a p-type dopant in WSe₂, and donates an extra hole to the system. [25,36,37] Charged trions, unlike neutral excitons experience stronger electrostatic interaction with the dopant impurities resulting in non-radiative recombination that quenches the PL intensity for vanadium concentrations >1.9%.[16,38] As expected, BEOL V-WSe₂ films display similar Raman and PL properties (Figure S5c,d, Supporting Information) as a function of vanadium concentration where the host lattice is perturbed after the dopant incorporation.

STM reveals a variety of uniformly distributed point defects in V-doped WSe₂ (Figure S6, Supporting Information). Several types of point defects were previously identified as either Re (\approx 32 ppm), Mo (\approx 340 ppm), or Cr (\approx 90 ppm) substituting for W,^[18,39] or as oxygen substituting for selenium (\approx 19 ppm),^[40] respectively. Consequently, we assign the most common point defect (0.43%), which appears as a dark depression at positive sample bias (**Figure 2a**) in the STM topography, as vanadium impurities. At negative sample bias, however, vanadium dopants appear as a bright protrusion (Figure 2b), indicative of a negatively charged (ionized) impurity.^[41] Indeed, Kelvin probe force microscopy (KPFM) experiments (Figure 2g) corroborate

V impurities to be negatively charged by the positive shift of the local contact potential difference (LCPD).^[42]

Combining STM and CO-tip noncontact atomic force microscopy (nc-AFM) confirms that V impurities substitutionally replace W atoms in the WSe₂ lattice (Figure 2d,e). The STS spectra of individual, relatively isolated V dopants (Figure 2c) reveal multiple in-gap states in the occupied spectrum, close to the valence band edge, in agreement with the expected formation of p-type defect states. At positive sample bias, the conduction band onset is pushed toward higher energies in the vicinity of dopants resulting from local band bending.[43] When the dopants are very close to each other, the defects exhibit a spectrum that is shifted toward higher energies (Figure S7c, Supporting Information), an electrostatic effect due to the negative defect charge analog to the negative energy shift observed for positively charged *n*-type dopants.^[18] This effect can be as large as several hundred millivolts, shifting the most tightly bound defect state up to the Fermi level.

Atomic resolution high angle annular dark field-STEM (HAADF-STEM) confirms the presence of vanadium atoms in the lattice (**Figure 3**a). The technique relies on atomic number based contrast difference^[44] where vanadium atoms are expected to exhibit reduced intensity as compared to W atoms owing to their smaller atomic number. The dopants (green dashed circles) are uniformly distributed throughout the WSe₂ lattice. The extrinsic films also contain other types of point defects such as single Se vacancies (red dashed circles) and double Se vacancies (cyan dashed circles) that are commonly observed in the WSe₂ lattice^[45] (Figure 3a) and attributed in part to beam-induced knock-on damage by the electron beam.^[46] Moreover, selected area electron diffraction (SAED) pattern exhibits single crystal

www.advancedsciencenews.com www.afm-journal.de

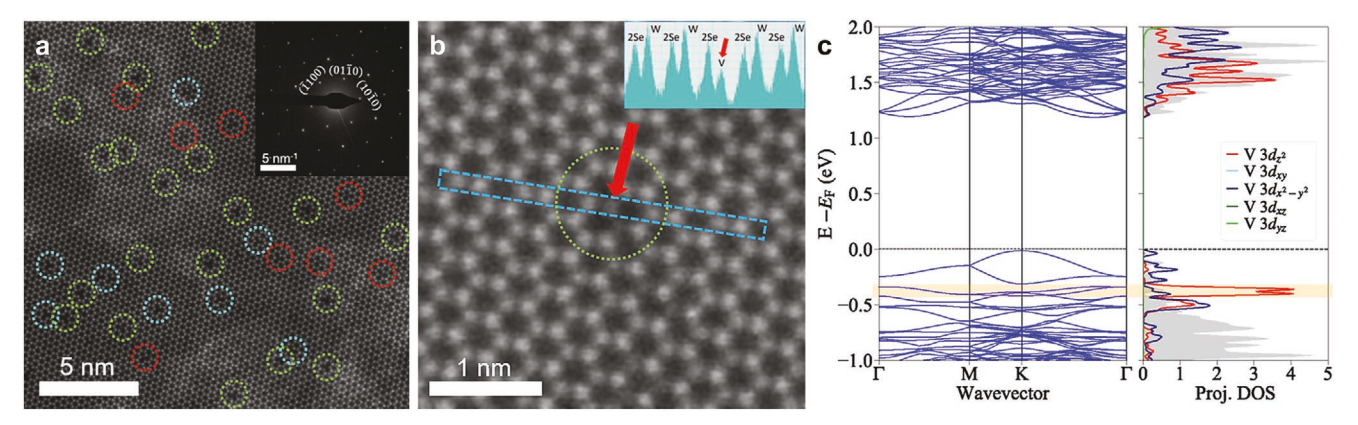


Figure 3. Atomic resolution imaging and DFT calculation of band structure, projected density of states and the possible position of vanadium dopants in the WSe₂ lattice. a) HAADF-STEM image showing V dopants (green dashed circles), single Se vacancies (red dashed circles) and double Se vacancies (cyan dashed circles) and SEAD pattern (inset) displaying single crystal nature of the films with hexagonal symmetry. b) Higher magnification HAADF-STEM image showing one V dopant atom where the blue box indicates an armchair direction along which the intensity profile is obtained (inset) highlighting the substitutional doping of the V dopant atom. c) Calculated band structure and projected density of states for the ionized V dopant on a W site, including spin—orbit coupling. The density of states is projected onto the *d*-orbitals of the V dopant atom, with the gray shading indicating the density of states for pristine WSe₂, for comparison. The most relevant defect state introduced by the V dopant near the top of the valence band is highlighted in the orange box.

signature with hexagonal symmetry (Figure 3a inset) indicating crystalline structure of V—WSe₂ films. An intensity line profile obtained along an armchair direction containing one V-dopant confirms the substitutional nature of the V dopant atom at the W site of the lattice (Figure 3b and inset) supporting our previous observations via XPS, Raman, and PL. This is evident from the low intensity peak corresponding to the V dopant atom whereas an adatom results in a higher intensity peak due to the combined intensity from W and V atoms. Furthermore, STEMenergy dispersive spectroscopy (EDS) mapping (Figure S8a-e, Supporting Information) underlines the uniform distribution of constituent elements in the film.

First-principles DFT calculations (see Experimental Section) confirm that the W site is the energetically most favorable site in the WSe₂ lattice for the V dopant (Table S1, Supporting Information), agreeing with the experimental findings. No significant atomic relaxations or symmetry breaking of the lattice in the vicinity of the dopant is observed in the calculations. The DFT-computed electronic band structure and density of states (Figure 3c) indicate that the V dopant introduces energy states (highlighted in orange) close to the top of the valence band. By projecting the density of states onto the individual *d*-orbitals of

the V dopant atom, this energy state is primarily from the V $3d_z^2$ orbital. When in the neutral (un-ionized) state, the dopant level is only partially occupied; however, the dopant is easily ionized, becoming negatively charged, and the fully filled dopant level falls slightly below the top of the valence band (Figure 3c) agreeing well with our experimental data and previous reports.^[37]

Transport measurements further corroborate the p-type nature of vanadium dopants. Back-gated field effect transistors (BGFETs) were fabricated on an Al₂O₃/Pt/TiN/p++-Si substrate using standard electron beam lithography process described elsewhere.[47,48] Transfer characteristics, that is, source to drain current (I_{DS}) as a function of back-gate voltage (V_{BG}) for different source to drain voltage (V_{DS}) of pristine and lightly doped (0.6%) WSe₂ show ambipolar characteristics (Figure 4a,b), with both n- and p-branches present. However, increasing the doping concentration to 1.1% and 1.9% (Figure 4c,d) leads to enhancement in the p-branch and reduction of the n-branch within the same $V_{\rm BG}$ measurement window. In other words, positive shift in the transfer characteristics or threshold voltage (V_{th}) of the p-branch with increasing V concentrations confirms the p-dopant nature of the V atoms in the WSe2, deduced from STM experiments and DFT simulations.

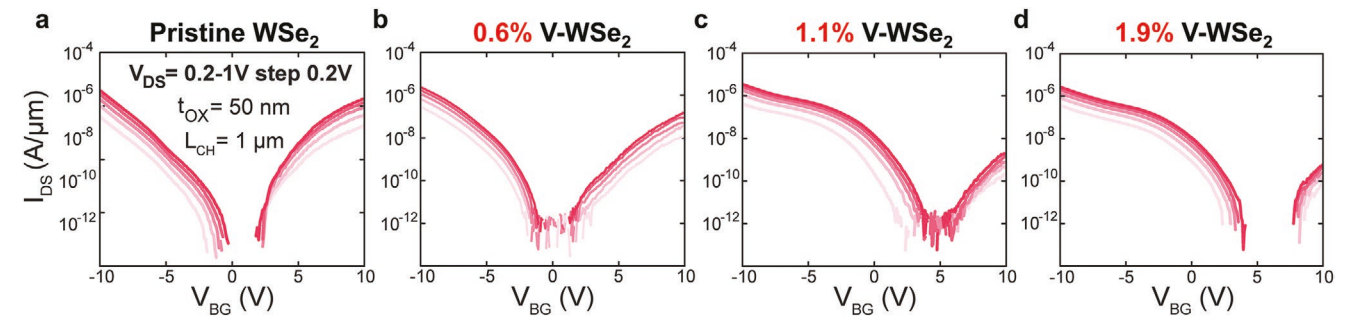


Figure 4. Transport properties of intrinsic and extrinsic FEOL WSe₂ BGFETs transferred on 50 nm ALD Al₂O₃ substrates. a) Transfer characteristics of the intrinsic films (I_{DS} vs V_{BG}) at a different drain voltages (V_{DS}) display expected ambipolar conduction. b–d) However, electron current (n-branch) starts to degrade as a function of vanadium concentration and BGFETs are no longer ambipolar and predominantly p-type.



www.advancedsciencenews.com



www.afm-journal.de

The hole mobility is extracted in the linear regime of the transfer curve using the peak transconductance method given by the equation:

$$\mu_h = \frac{dI_{DS}}{dV_{BG}} \left(\frac{W}{L_{CH}} C_{ox} V_{DS} \right)^{-1} \tag{1}$$

where W is the width, L_{CH} is the length of the channel, C_{ox} is the gate capacitance per unit area given as $C_{ox} = \frac{\varepsilon_0 \varepsilon_{ox}}{t_{ox}}$, where ε_0 is the dielectric constant of free space, ε_{ox} is the dielectric constant of Al₂O₃, and t_{ox} is the thickness of the gate dielectric. The threshold voltage (V_{th}) was extracted using the constant current method for $I_{\rm DS}=100~{\rm nA~\mu m^{-1}}$ (Table S2, Supporting Information). All the constructed devices (Table S2, Supporting Information) display ON-OFF ratio (I_{ON}/I_{OFF}) exceeding 10⁶ and mobility values similar to previous reports. [25,49] Improvement in the I_{ON} for the p channel, without losing gate modulation, further highlights the effectiveness of vanadium for p-doping of large-area 2D WSe2 at FEOL and BEOL compatible temperatures.

3. Conclusion

The scalable vanadium doping of 2D WSe2 is readily achievable via MOCVD at FEOL and BEOL compatible temperatures. Our experimental findings confirm the successful incorporation of the dopants by substitutionally replacing W atoms in the host lattice where the concentration of vanadium atoms can be precisely tuned by having accurate control over the vanadium precursor flux. Atomic-scale characterization reveals that the dopants are uniformly distributed throughout the WSe₂ lattice. Moreover, incorporated V atoms introduce discrete energy levels within the band gap of WSe2, located in proximity to its valence band and thus confirm the expected p-type nature of the dopants. Ultimately, the integration of 2D materials with Si CMOS will require wafer-scale production of intrinsic and extrinsic materials at various temperatures with the highest precision. In this context, the method introduced in the current study will help to bridge the gap between academia and industry.

4. Experimental Section

MOCVD Growth of Pristine and V-Doped WSe2 Films: A customdesigned vertical cold wall gas-source CVD reactor was utilized to synthesize intrinsic and extrinsic WSe₂ films as previously reported.^[11,18] The tungsten hexacarbonyl (W(CO)₆) (99.99%, Sigma-Aldrich), Bis (cyclopentadienyl) vanadium $(V(C_5H_5)_2)$ (sublimed, 95%, Strem Chemicals), and hydrogen selenide (H₂Se) (99.99% Matheson) were used as metal, dopant, and chalcogen precursors, respectively in a 100% H₂ ambient. The solid-state metal and dopant sources were kept inside the stainless-steel bubblers where temperature and pressure of the bubblers were constantly maintained at 25 $^{\circ}\text{C}$ and 725 Torr, and 40 °C and 725 Torr, respectively. Hydrogen selenide was supplied from a different gas manifold and all three precursors were introduced from separate lines to prevent the intermixing before reaching the reactor inlet. The three-step growth (nucleation, ripening, and lateral growth) method^[8] was used to grow monolayer, epitaxial intrinsic, and extrinsic FEOL WSe₂ on c-plane sapphire (Cryscore Optoelectronic Ltd, 99.996%) substrates. Growth temperature, pressure, and H2Se flow rate were kept constantly at 800 °C, 700 Torr, and 7 sccm, respectively, for all three growth steps. At the nucleation stage, the metal and the dopant precursors were introduced simultaneously with a flow rate of 20 and 60 sccm, respectively, for 2 min. At the ripening stage, W(CO)₆ and V₂(C₅H₅) were switched off and formed V-WSe₂ nuclei were let anneal under H₂Se for 10 min. W(CO)₆ was re-introduced with a constant 4.5 sccm at the lateral growth stage (30 min), whereas the dopant flow rate varied from 30 to 5 sccm depending on the desired vanadium content in the films. After the ripening stage, the metal and dopant sources were cut-off and post-growth annealing under H2Se was carried out for 10 min and followed by cooling down to room temperature. The BEOL counterparts were synthesized with a single-step growth method on SiO₂/Si substrates (University Wafer, Silicon P/B (100)) with 300 nm wet thermal oxide where the temperature and pressure of the reaction chamber were kept at 400 °C and 700 Torr, respectively.[11,18] To promote the lateral growth of the pristine and V-WSe2 films at this kinetically limited growth regime, the precursors flow rates were adjusted accordingly to 2 and 9 sccm for W(CO)₆ and H₂Se, respectively whereas the $V_2(C_5H_5)$ flow rate was varied from 10 to 2.5 sccm. At both FEOL and BEOL conditions, the dopant concentration was a direct function of the $(V(C_5H_5)_2)$ partial pressure where increasing the flow rate of the vanadium precursor resulted in a monotonic increase on the dopant concentration in the films. Within the investigated window of vanadium dopant concentrations, no saturation of the dopant concentration was observed at both FEOL and BEOL growth temperatures. Prior to the growth, sapphire and SiO₂/Si substrates were cleaned with acetone and isopropyl alcohol in an ultrasonication bath for 10 min each followed by deionized (DI) water rinse and N2 gun dry. To further minimize the organic contamination on the surface, the substrates were cleaned with commercially available heated Piranha solution (Nanostrip, KMG Electronic Chemicals) at 90 °C for 20 min and rinsed with DI water.

Atomic Force Microscopy: Bruker Icon I tool was used to acquire AFM data in a peak force tapping mode.

Raman and PL Spectroscopy: Raman and PL spectra of the samples were obtained by the Horiba Labram HR Evolution VIS-NIR Raman system with a 633 nm laser at 0.4 mW power and 532 nm laser at 0.4 mW power, respectively.

Scanning Electron Microcopy: Verios G4 with the accelerating voltage of 2 keV was employed to analyze the films.

X-Ray Photoelectron Spectroscopy: High-resolution XPS data was obtained by a Physical Electronics Versa Probe II tool with a monochromatic Al K_{α} X-ray source (h ν = 1486.7 eV) at high vacuum (<10⁻⁶ Torr) environment. The acquired spectra were charge corrected to C1s core level at 284.8 eV and W $4f_{7/2}$ at 32.7 eV, respectively. U 2 Tougaard background was used for V and W whereas Iterated Shirley background was used for Se to fit the XPS spectra of the samples. The concentration of the vanadium dopants were quantified via the Casa XPS software where the peak area and intensity of the V 2p region were taken to account relative to W and Se regions.

STM, STS, nc-AFM, and KPFM: V-doped WSe2 FEOL samples were prepared ex situ on EG on SiC substrates followed by a final 450 °C anneal in ultrahigh vacuum. The measurements were performed with a commercial QPlus from Scienta Omicron operated at 5 K and at pressures below $2\times10^{-10}\ \text{mbar}.$ For STM, STS, and KPFM, the tungsten tip mounted on a QPlus tuning fork sensor was prepared on a clean Au(111) surface (sputtering: 10 min, Ar+, 1kV; annealing: 10 min, 450 °C) and confirmed to be metallic. For nc-AFM experiments, the metallic tip was modified with a single CO molecule $^{[50]}$ that was picked up from Au(111) surface. STM topographic measurements were taken in constant current mode with the bias voltage given with respect to the sample. STS measurements were recorded using a lock-in amplifier at 610 Hz and modulation amplitude of 20 meV. The nc-AFM topographies and KPFM measurements were acquired in constant height mode, while the QPlus sensor was driven at its resonance frequency (of ≈25 kHz) with a constant amplitude of 70 pm. The frequency shift from resonance of the tuning fork was recorded using Omicron Matrix electronics and HF₂Li PLL from Zurich Instruments.



www.advancedsciencenews.com



____MATERIALS

Transmission Electron Microscopy: As grown V—WSe₂ films were lifted from sapphire substrates and transferred to Quantifoil Cu TEM grids using a PMMA assisted transfer method.^[51] SAED patterns and STEM-EDS maps were acquired using a Thermo Fisher Talos F200X instrument at 80 kV acceleration voltage. A Thermo Fisher Tian³ G2 microscope equipped with image and probe correctors was employed to collect atomic resolution HAADF-STEM data. The images were acquired using 30 mrad semi convergence angle, ≈50 pA screen current and 80 kV acceleration voltage to minimize the possible damage to the samples. Acquired atomic resolution images were smoothed with a 2-pixel Gaussian blur filter using ImageJ where brightness and contrast of the images were adjusted accordingly.

DFT Calculations: The formation energy and electronic structure of the substitutional V dopant was computed using DFT as implemented in the Vienna ab initio simulation package VASP. [52] Calculations were performed using projector-augmented wave potentials [53,54] with Perdew–Burke–Ernzerhof[55] generalized gradient approximation functionals to treat the exchange-correlation. Spin-polarized calculations with spin-orbit coupling were performed with a plane wave cutoff energy of 520 eV, Methfessel–Paxton smearing [56] with a smearing energy width of 0.10 eV, and Γ -centered Monkhorst–Pack k-point meshes [57] for Brillouin zone integration. The dopant was modeled using 4 × 4 and 5 × 5 supercells containing a single dopant atom each, and 20 Å vacuum spacing between layers to minimize interlayer interaction.

The formation energy $E^f[X]$ of a neutral point defect X was determined from DFT calculations using a supercell approach following $E^f[X] = E_{tot}[X] - E_{tot}[pristine] - \Sigma_i \ n_i \mu_i$, where $E_{tot}[X]$ and $E_{tot}[pristine]$ are the total DFT-computed energies of the supercell containing the defect X and the pristine supercell, respectively, n_i is the number of atoms of species i added/removed, and μ_i is the corresponding chemical potential of the species. The values reported in this work were referenced to bcc V for μV , and either bcc W for μW (W-rich limit), or hexagonal (gray) Se for μ_{Se} (Se-rich limit).

Fabrication of Field Effect Transistors: The as-grown pristine and V-doped WSe2 films were transferred onto a 50 nm ALD Al2O3 on Pt/TiN/p++ Si from the host c-plane sapphire substrates. Photoresist was spun and 1 μm by 5 μm strips of V-WSe2 were isolated from the conformal film using e-beam lithography (EBPG 5200 Vistec). After developing, a Plasma-Therm Versalock 700 inductively coupled plasma etch tool was used (SF6/O2 30/10 sccm gas mixture) to remove the exposed film. Photoresist was spun and source and drain contacts were defined using e-beam lithography, followed by 40 nm Ni and 30 nm Au contact metal deposition in a Temescal e-beam evaporator tool. The electrical characterization was conducted using a Keysight B1500A semiconductor parameter analyzer; the measurements were done at room temperature and at $\approx 10^{-5}$ Torr.

Supporting Information

Supporting Information is available from the Wiley Online Library or from the author.

Acknowledgements

A.K. and J.A.R. acknowledge Intel through the Semiconductor Research Corporation (SRC) Task 2746, the Penn State 2D Crystal Consortium (2DCC)-Materials Innovation Platform (2DCC-MIP) under NSF cooperative agreement DMR- 1539916, and NSF CAREER Award 1453924 for financial support. S.S. acknowledges funding from the Swiss National Science Foundation under SNSF project number 159690. A.M.Z.T. and R.G.H. were also funded by the NSF through the 2DCC-MIP under award DMR-1539916, and by additional awards DMR-1748464 and OAC-1740251. Computational resources were provided by the University of Florida Research Computing Center. The work of R.P. and S.D was supported by Army Research Office (ARO) through Contract Number

W911NF1920338. S.B. and N.A. also acknowledge additional support provided by NSF CAREER DMR-1654107 and Materials Characterization Lab at Penn State.

Conflict of Interest

The authors declare no conflict of interest.

Data Availability Statement

Research data are not shared.

Keywords

doping, metal-organic chemical vapor deposition, tungsten diselenide, 2D materials, vanadium doping

Received: June 1, 2021 Revised: July 2, 2021 Published online: July 23, 2021

- [1] Y. Liu, X. Duan, H. Shin, S. Park, Y. Huang, X. Duan, *Nature* **2021**, *591*, 43.
- [2] D. Akinwande, C. Huyghebaert, C. H. Wang, M. I. Serna, S. Goossens, L. J. Li, H. S. P. Wong, F. H. L. Koppens, *Nature* 2019, 573, 507.
- [3] I. Asselberghs, Q. Smets, T. Schram, B. Groven, D. Verreck, G. Afzalian, G. Arutchelvan, A. Gaur, D. Cott, T. Maurice, S. Brems, K. Kennes, A. Phommahaxay, E. Dupuy, D. Radisic, J. De Marneffe, A. Thiam, W. Li, K. Devriendt, C. Huyghebaert, D. Lin, M. Caymax, P. Morin, I. P. Radu, IEEE Int. Electron Devices Meet. 2020, 40.2.1.
- [4] Z. Ahmed, A. Afzalian, T. Schram, D. Jang, D. Verreck, Q. Smets, P. Schuddinck, B. Chehab, S. Sutar, G. Arutchelvan, A. Soussou, I. Asselberghs, A. Spessot, I. P. Radu, B. Parvais, J. Ryckaert, M. H. Na, IEEE Int. Electron Devices Meet. 2020, 22.5.1.
- [5] C. Lo, B. A. Helfrecht, Y. He, D. M. Guzman, N. Onofrio, S. Zhang, J. Appl. Phys. 2020, 128, 080903.
- [6] J. A. Robinson, APL Mater. 2018, 6, 058202.
- [7] A. Kozhakhmetov, R. Torsi, C. Y. Chen, J. A. Robinson, J. Phys. Mater. 2020, 4, 012001.
- [8] X. Zhang, T. H. Choudhury, M. Chubarov, Y. Xiang, B. Jariwala, F. Zhang, N. Alem, G. C. Wang, J. A. Robinson, J. M. Redwing, *Nano Lett.* 2018, 18, 1049.
- [9] M. Seol, M. H. Lee, H. Kim, K. W. Shin, Y. Cho, I. Jeon, M. Jeong, H. I. Lee, J. Park, H. J. Shin, Adv. Mater. 2020, 32, 2003542.
- [10] M. Chubarov, T. H. Choudhury, D. R. Hickey, S. Bachu, T. Zhang, A. Sebastian, A. Bansal, H. Zhu, N. Trainor, S. Das, M. Terrones, N. Alem, J. M. Redwing, ACS Nano 2021, 15, 2532.
- [11] A. Kozhakhmetov, J. R. Nasr, F. Zhang, K. Xu, N. C. Briggs, R. Addou, R. Wallace, S. K. Fullerton-Shirey, M. Terrones, S. Das, J. A. Robinson, 2D Mater. 2020, 7.
- [12] H. Medina, J.-G. Li, T.-Y. Su, Y.-W. Lan, S.-H. Lee, C.-W. Chen, Y.-Z. Chen, A. Manikandan, S.-H. Tsai, A. Navabi, X. Zhu, Y.-C. Shih, W.-S. Lin, J.-H. Yang, S. R. Thomas, B.-W. Wu, C.-H. Shen, J.-M. Shieh, H.-N. Lin, A. Javey, K. L. Wang, Y.-L. Chueh, *Chem. Mater.* 2017, 29, 1587.
- [13] J. Mun, Y. Kim, I. S. Kang, S. K. Lim, S. J. Lee, J. W. Kim, H. M. Park, T. Kim, S. W. Kang, Sci. Rep. 2016, 6, 1.



www.advancedsciencenews.com www.afm-journal.de

ADVANCED FUNCTIONAL MATERIALS

- [14] A. Kozhakhmetov, T. H. Choudhury, Z. Y. Al Balushi, M. Chubarov, J. M. Redwing, J. Cryst. Growth 2018, 486, 137.
- [15] A. J. Arnold, D. S. Schulman, S. Das, ACS Nano 2020, 14, 13557.
- [16] D. H. Lien, S. Z. Uddin, M. Yeh, M. Amani, H. Kim, J. W. Ager, E. Yablonovitch, A. Javey, *Science* 2019, 364, 468.
- [17] P. Luo, F. Zhuge, Q. Zhang, Y. Chen, L. Lv, Y. Huang, H. Li, T. Zhai, Nanoscale Horiz. 2019, 4, 26.
- [18] A. Kozhakhmetov, B. Schuler, A. M. Z. Tan, K. A. Cochrane, J. R. Nasr, H. El-Sherif, A. Bansal, A. Vera, V. Bojan, J. M. Redwing, N. Bassim, S. Das, R. G. Hennig, A. Weber-Bargioni, J. A. Robinson, Adv. Mater. 2020, 32, 2005159.
- [19] Y. C. Lin, R. Torsi, D. B. Geohegan, J. A. Robinson, K. Xiao, Adv. Sci. 2021, 8, 2004249.
- [20] M. Li, B. Cai, R. Tian, X. Yu, M. B. H. Breese, X. Chu, Z. Han, S. Li, R. Joshi, A. Vinu, T. Wan, Z. Ao, J. Yi, D. Chu, *Chem. Eng. J.* 2021, 409 128158
- [21] L. Zhang, G. Wang, Y. Zhang, Z. Cao, Y. Wang, T. Cao, C. Wang, B. Cheng, W. Zhang, X. Wan, J. Lin, S. J. Liang, F. Miao, ACS Nano 2020, 14, 10265.
- [22] J. Zou, Z. Cai, Y. Lai, J. Tan, R. Zhang, S. Feng, G. Wang, J. Lin, B. Liu, H. M. Cheng, ACS Nano 2021, 15, 7340.
- [23] J. Jiang, L. A. T. Nguyen, T. D. Nguyen, D. H. Luong, D. Y. Kim, Y. Jin, P. Kim, D. L. Duong, Y. H. Lee, *Phys. Rev. B* **2021**, *103*, 014441.
- [24] S. Li, J. Hong, B. Gao, Y. C. Lin, H. E. Lim, X. Lu, J. Wu, S. Liu, Y. Tateyama, Y. Sakuma, K. Tsukagoshi, K. Suenaga, T. Taniguchi, Adv. Sci. 2021, 8, 2004438.
- [25] S. J. Yun, D. L. Duong, D. M. Ha, K. Singh, T. L. Phan, W. Choi, Y. M. Kim, Y. H. Lee, Adv. Sci. 2020, 7, 1903076.
- [26] H. Gao, J. Suh, M. C. Cao, A. Y. Joe, F. Mujid, K. H. Lee, S. Xie, P. Poddar, J. U. Lee, K. Kang, P. Kim, D. A. Muller, J. Park, *Nano Lett.* 2020, 20, 4095.
- [27] L. M. Dyagileva, V. P. Mar'in, E. I. Tsyganova, G. A. Razuvaev, J. Organomet. Chem. 1979, 175, 63.
- [28] J. R. Shallenberger, Surf. Sci. Spectra 2018, 25, 014001.
- [29] M. Hossain, J. Wu, W. Wen, H. Liu, X. Wang, L. Xie, Adv. Mater. Interfaces 2018, 5, 1800528.
- [30] G. Hopfengärtner, D. Borgmann, I. Rademacher, G. Wedler, E. Hums, G. W. Spitznagel, J. Electron Spectrosc. Relat. Phenom. 1993, 63, 91.
- [31] N. D. Boscher, C. S. Blackman, C. J. Carmalt, I. P. Parkin, A. G. Prieto, Appl. Surf. Sci. 2007, 253, 6041.
- [32] W. Zhao, Z. Ghorannevis, K. K. Amara, J. R. Pang, M. Toh, X. Zhang, C. Kloc, P. H. Tan, G. Eda, *Nanoscale* 2013, 5, 9677.
- [33] E. Del Corro, H. Terrones, A. Elias, C. Fantini, S. Feng, M. A. Nguyen, T. E. Mallouk, M. Terrones, M. A. Pimenta, ACS Nano 2014, 8, 9629.

- [34] W. Shi, M. L. Lin, Q. H. Tan, X. F. Qiao, J. Zhang, P. H. Tan, 2D Mater. 2016, 3, 025016.
- [35] Q. Qian, Z. Zhang, K. J. Chen, Langmuir 2018, 34, 2882.
- [36] S. Mouri, Y. Miyauchi, K. Matsuda, Nano Lett. 2013, 13, 5944.
- [37] S. J. Yun, Y. Kim, S. Kim, Y. H. Lee, Appl. Phys. Lett. 2019, 115, 242406.
- [38] K. F. Mak, K. He, C. Lee, G. H. Lee, J. Hone, T. F. Heinz, J. Shan, Nat. Mater. 2013, 12, 207.
- [39] B. Schuler, J. H. Lee, C. Kastl, K. A. Cochrane, C. T. Chen, S. Refaely-Abramson, S. Yuan, E. Van Veen, R. Roldán, N. J. Borys, R. J. Koch, S. Aloni, A. M. Schwartzberg, D. F. Ogletree, J. B. Neaton, A. Weber-Bargioni, ACS Nano 2019, 13, 10520.
- [40] S. Barja, S. Refaely-Abramson, B. Schuler, D. Y. Qiu, A. Pulkin, S. Wickenburg, H. Ryu, M. M. Ugeda, C. Kastl, C. Chen, C. Hwang, A. Schwartzberg, S. Aloni, S. K. Mo, D. F. Ogletree, M. F. Crommie, O. V. Yazyev, S. G. Louie, J. B. Neaton, A. Weber-Bargioni, *Nat. Commun.* 2019, 10, 3382.
- [41] P. Mallet, F. Chiapello, H. Okuno, H. Boukari, M. Jamet, J. Y. Veuillen, Phys. Rev. Lett. 2020, 125, 036802.
- [42] L. Gross, F. Mohn, P. Liljeroth, J. Repp, F. J. Giessibl, G. Meyer, Science 2009, 324, 1428.
- [43] M. Aghajanian, B. Schuler, K. A. Cochrane, J. H. Lee, C. Kastl, J. B. Neaton, A. Weber-Bargioni, A. A. Mostofi, J. Lischner, Phys. Rev. B 2020, 101, 081201.
- [44] O. L. Krivanek, M. F. Chisholm, V. Nicolosi, T. J. Pennycook, G. J. Corbin, N. Dellby, M. F. Murfitt, C. S. Own, Z. S. Szilagyi, M. P. Oxley, S. T. Pantelides, S. J. Pennycook, *Nature* 2010, 464, 571.
- [45] N. Nayir, Y. Wang, S. Shabnam, D. Reifsnyder Hickey, L. Miao, X. Zhang, S. Bachu, N. Alem, J. Redwing, V. H. Crespi, A. C. T. van Duin, J. Phys. Chem. C 2020, 124, 28285.
- [46] S. Wang, A. Robertson, J. H. Warner, Chem. Soc. Rev. 2018, 47, 6764.
- [47] D. Jayachandran, A. Oberoi, A. Sebastian, T. H. Choudhury, B. Shankar, J. M. Redwing, S. Das, *Nat. Electron.* 2020, 3, 646.
- [48] A. Sebastian, R. Pendurthi, T. H. Choudhury, J. M. Redwing, S. Das, Nat. Commun. 2021, 12, 693.
- [49] S. Fan, S. J. Yun, W. J. Yu, Y. H. Lee, Adv. Sci. 2019, 7, 1902751.
- [50] F. Mohn, B. Schuler, L. Gross, G. Meyer, Appl. Phys. Lett. 2013, 102, 073109
- [51] K.-K. Liu, W. Zhang, Y.-H. Lee, Y.-C. Lin, M.-T. Chang, C.-Y. Su, C.-S. Chang, H. Li, Y. Shi, H. Zhang, C.-S. Lai, L.-J. Li, Nano Lett. 2012, 12, 1538.
- [52] G. Kresse, J. Furthmüller, Phys. Rev. B 1996, 54, 11169.
- [53] P. E. Blöchl, Phys. Rev. B 1994, 50, 17953.
- [54] G. Kresse, D. Joubert, Phys. Rev. B 1999, 59, 1758.
- [55] J. P. Perdew, K. Burke, M. Ernzerhof, Phys. Rev. Lett. 1996, 77, 3865.
- [56] M. Methfessel, A. T. Paxton, Phys. Rev. B 1989, 40, 3616.
- [57] H. J. Monkhorst, J. D. Pack, Phys. Rev. B 1976, 13, 5188.